Extraordinary role of Zn in enhancing thermoelectric performance of Ga-doped n-type PbTe

Journal:	*Energy & Environmental Science*
Manuscript ID	EE-ART-09-2021-002986.R2
Article Type:	Paper
Date Submitted by the Author:	05-Dec-2021
Complete List of Authors:	Luo, Zhong-zhen; Northwestern University, Department of Chemistry
	Cai, Songting; Northwestern University, Material Science and Engineering
	Hao, Shiqiang; Northwestern University, Materials Science
	Bailey, Trevor; University of Michigan, Department of Physics
	Luo, Yubo; Nanyang Technological University, School of materials science and engineering
	Luo, Wenjun; Nanjing University, ; Nanjing Tech University,
	Yu, Yan; Fuzhou University
	Uher, Ctirad; University of Michigan, Department of Physics
	Wolverton, Chris; Northwestern University, Department of Materials Science and Engineering
	Dravid, Vinayak; Northwestern University, Materials Science & Engineering
	Zou, Zhigang; Nanjing University, Physics
	Yan, Qingyu; Nanyang Technological University, MSE
	Kanatzidis, Mercouri; Northwestern University, Department of Chemistry

Extraordinary role of Zn in enhancing thermoelectric performance of Ga-doped n-type PbTe

Zhong-Zhen Luo,[1,2,3,4] Songting Cai,[4,5] Shiqiang Hao,[5] Trevor P. Bailey,[6] Yubo Luo,[3,4,7] Wenjun Luo,[2,8] Yan Yu,[1,2] Ctirad Uher,[6] Christopher Wolverton,[5] Vinayak P. Dravid,[5] Zhigang Zou,[1,2,8,*] Qingyu Yan,[3,*] Mercouri G. Kanatzidis[4,*]

[1]Key Laboratory of Eco-materials Advanced Technology, College of Materials Science and Engineering, Fuzhou University, Fuzhou, 350108, China

[2]Fujian Science & Technology Innovation Laboratory for Optoelectronic Information of China, Fuzhou, Fujian 350108, P. R. China

[3]School of Materials Science and Engineering, Nanyang Technological University, 50 Nanyang Avenue 639798, Singapore

[4]Department of Chemistry, Northwestern University, Evanston, Illinois 60208, United States

[5]Department of Materials Science and Engineering, Northwestern University, Evanston, Illinois 60208, United States

[6]Department of Physics, University of Michigan, Ann Arbor, Michigan 48109, United States

[7]State Key Laboratory of Materials Processing and Die & Mould Technology, School of Materials Science and Engineering, Huazhong University of Science and Technology, Wuhan 430074, P. R. China

[8]Eco-materials and Renewable Energy Research Center, College of Engineering and Applied Sciences, Nanjing University, Nanjing, 210093, China

ABSTRACT

Although Ga doping can weaken the electron phonon coupling of n-type PbTe, Ga-doped PbTe has a relatively low carrier concentration (n) and high lattice thermal conductivity (κ_{lat}), resulting in a lower figure of merit (ZT) compared with those of other top-performing n-type PbTe-based thermoelectric materials. Herein, we report the extraordinary role of Zn in enhancing the thermoelectric performance of Ga-doped PbTe. It is discovered that Zn can simultaneously improve the electronic transport properties and decrease the κ_{lat} of Ga-doped PbTe, thereby affording a record high ZT_{avg} ~1.26 at 400–873 K, with a maximum ZT value of 1.55 at 723 K. The isoelectronic substitution of Zn for Pb in Ga-doped PbTe increases the electrical conductivity and n by inducing the nucleation and growth of Ga_2Te_3 in the second phase. The formation of Ga_2Te_3 results in nonstoichiometric and Te deficiency in the

PbTe matrix, which increases the number of electron carriers. Additionally, discordant Zn and Ga atoms with the highest displacement of ~0.35 Å for Zn alloying, as well as Ga_2Te_3 nanocrystals ranging from 30 to 200 nm coherently embedded into the PbTe matrix effectively weaken the phonon modes and scatter heat-carrying phonons, resulting in a significant reduction in κ_{lat}.

Key Words: Thermoelectric; N-type PbTe; Ga_2Te_3 nanocrystals; Discordant Zn atoms; Thermal conductivity

INTRODUCTION

More than two-thirds of the globally generated energy is dissipated in the form of waste heat.[1] Solid-state technology that can capture and convert heat energy from various sources into useful forms, such as electricity, is of considerable interest.[1-3] Thermoelectric technology can convert waste heat while affording advantages of small dimensions, long steady-state operation periods, zero gas emissions, and no moving components. The conversion efficiency (η) of thermoelectric materials can be expressed using a dimensionless figure of merit, $ZT = S^2\sigma T/(\kappa_{lat} + \kappa_{ele})$, where S, σ, T, κ_{lat}, and κ_{ele} represent the Seebeck coefficient, electrical conductivity, operating temperature (in Kelvin), lattice thermal conductivity, and electronic thermal conductivity, respectively.[4-6] Because these properties are generally strongly coupled, a high ZT is difficult to obtain. Furthermore, the efficiency (η_{dev}) of the device depends directly on the average ZT ($ZT_{avg} = \frac{1}{T_H-T_C}\int_{T_C}^{T_H} ZT dT$), i.e., $\eta_{dev} = [(T_H - T_C)/T_H] [(1 + ZT_{avg})^{1/2} - 1]/[(1 + ZT_{avg})^{1/2} + T_C/T_H]$, where T_H and T_C are the hot- and cold-side temperatures of the device, respectively.[7]

PbTe is recognized as one of the most important intermediate temperature materials for thermoelectric power generation.[8] The thermoelectric performance of thermoelectric materials can be improved via one of two primary approaches: enhancing the power factor via favorable band-structure modification (including multiband convergence[9-12] and midgap states[13]) and reducing κ_{lat} via alloying (including designed nanostructures,[7] dislocations,[14] and all-length-scale hierarchical architectures[15]). The extraordinary performance of p-type PbTe with $ZT \geqslant 2$ has been achieved by employing band convergence and enhanced phonon scattering strategies.[14, 16, 17] Typically, n-type PbTe thermoelectric materials are inferior to their p-type counterparts because of their inability to benefit from band convergence. This is because of their larger energy offset (ΔE_v ~0.45 eV) of light (L point) and heavy (Σ point) conduction bands compared with that of ~0.15–0.20 eV for the valence band.[18] Consequently, the Seebeck coefficient of PbTe for n-type samples is lower than those for p-type ones for similar carrier concentrations, n.[19] Hence, high-performing n-type

PbTe thermoelectric materials are to be further developed for the advancement of thermoelectric device assembly and application.

Recently, Ga doping has been shown to weaken the electron–phonon coupling of n-type PbTe.[20] However, the latter has a relatively low n compared with other n-type samples with dopants such as I,[21] La,[22] Sb,[19] and Bi[19] (Figure S1, Supporting Information). Furthermore, it has a high κ_{lat} ~0.8 $Wm^{-1}K^{-1}$, which is much higher than the minimum theoretical value for PbTe (~0.36 $Wm^{-1}K^{-1}$). We previously demonstrated that GeTe alloying can effectively reduce κ_{lat} and improve ZT, although the n and electrical conductivity are decreased.[13] Theoretically, isovalent element alloying strategies will result in a constant n accompanied by lower mobility and electrical conductivity. In practice, substitutions such as Sr,[23] Mg,[15] Cd,[24] Hg,[24] Zn,[25] Ge[7] and S,[16] in both n- and p-type PbTe samples tend to decrease the electrical conductivity because of the enhanced scattering of charge carriers, i.e., reduced electronic mobility.[26] To date, the simultaneous reduction in the κ_{lat} and increase in the n and electrical conductivity of Ga-doped PbTe has not been reported.

In this study, we synthesized a series of $Pb_{0.975}Ga_{0.025}Te–x\%ZnTe$ compounds via vacuum melting followed by spark plasma sintering. Previous reports show that the substitution of Zn into the PbTe matrix does not affect n but decreases the electrical conductivity of I-doped n-type PbTe.[25] However, for Ga-doped PbTe, Zn with the largest displacement of ~0.35 Å in the PbTe matrix simultaneously optimized the electrical and thermal transport. It was observed that n nearly doubled with less than 1% Zn isoelectronic substitution of Pb. By contrast, a 0.5% Zn substitution resulted in a ~26% reduction in κ_{lat} as compared with that afforded by Ga-doped PbTe owing to the soft phonon modes from discordant Zn and Ga atoms. Consequently, a record high ZT_{avg} of ~1.26 at 400–873 K with a maximum ZT value of 1.55 at 723 K was obtained.

RESULTS AND DISCUSSION

Structural characterization and optical properties To verify the solubility of Zn in the PbTe matrix, the powder X-ray diffraction (PXRD) patterns of PbTe–x%ZnTe (x

= 0, 0.5, 1, 2, and 3) are shown in Figure S2 (Supporting Information). The samples crystallized in the rock-salt type structure, which matched the cubic PbTe structure with a space group of $Fm\bar{3}m$ (JCPDS 78−1905). No secondary phase was detected (for x ≤ 2). However, in the x = 3 sample, the reflection peaks originating from ZnTe at ~25° and 42° were detected. The values of the lattice parameters calculated from the PXRD patterns decreased gradually as ZnTe content increased from x = 0.5 to 1; beyond that value, it remained almost unchanged (Figure S3, Supporting Information). The lattice contraction was due to the smaller atomic radius of Zn^{2+} (~0.74 Å) compared with that of Pb^{2+} (~1.20 Å), indicating the substitution of Pb with Zn in the lattice with a solubility limit of Zn in PbTe of less than 2%, which is consistent with a previous study.[27, 28] Hence, we selected a Zn content of less than 1% and added Ga as the n-type dopant. As shown in Figure S4 (Supporting Information), the PXRD patterns of $Pb_{0.975}Ga_{0.025}Te–x\%ZnTe$ (x = 0, 0.25, 0.5, 0.75, and 1) show no additional significant peaks. However, the weak peaks that appeared near the (002) and (022) peaks for the $Pb_{0.975}Ga_{0.025}Te–0.75\%ZnTe$ sample (as shown in Figure S5a (Supporting Information)) indicate the reduced solid solubility of ZnTe, which is caused by Ga doping and the generation of Ga_2Te_3 secondary phase in the samples at x > 0.5%. The values of the lattice parameters of $Pb_{0.975}Ga_{0.025}Te–x\%ZnTe$ decreased gradually with increasing ZnTe (Figure S5b, Supporting Information).

As shown in Figure S6 (Supporting Information), the electronic band gaps of PbTe–x%ZnTe increased slightly from ~0.24 eV for pure PbTe to ~0.29 eV for the 2% ZnTe-alloyed sample. This increase can be attributed to the wider band gap of ZnTe (i.e., 2.25 eV).[29]

Charge-transport properties As shown in Figure 1a, the substitution of ZnTe for Ga-doped PbTe consistently decreased the magnitude of the n-type Hall coefficients, R_H, and consequently increased n. Both trends with respect to the ZnTe content were consistent with the electrical conductivity and Seebeck coefficient data, as will be discussed below. Moreover, as shown in Figure 1c, the carrier mobility μ_H of $Pb_{0.975}Ga_{0.025}Te–x\%ZnTe$ is generally higher than that of other top-performing n-type

PbTe-based systems (i.e., PbTe–InSb,[30] $Cu_{m+n}Pb_{100}Sb_mTe_{100}Se_{2m}$,[31] PbTe–$La_2Te_3$,[32] $PbTe_{1-x}I_{x-y}MgTe1\%$,[33] PbTe–GaSb[34] and $Pb_{1-x}Sn_xTe_{0.997-y}Se_yI_{0.003}$[35]) at room temperature. The temperature dependences of R_H and n for $Pb_{0.975}Ga_{0.025}Te$–0.25%ZnTe are shown in Figure 1b. As the temperature increased to approximately 450 K, the Hall coefficient increased to a maximum before gradually declining at higher temperatures owing to the thermally activated behavior of Ga^+ (Figure S8, Supporting Information).[13]

The electrical conductivity of the $Pb_{0.975}Ga_{0.025}Te$–x%ZnTe samples decreased with increasing temperature for all samples, which is characteristic of degenerate semiconductors (Figure 2a). However, the electrical conductivity increased with the ZnTe content. Specifically, the sample with x = 0.5 indicated the highest electrical conductivity of ~2941 S cm^{-1} at room temperature compared with 1870 S cm^{-1} of the sample with x = 0. The significant increase in electrical conductivity via isoelectronic substitution of Zn to Pb is counterintuitive and is in contrast to the previous I-doped PbTe–ZnTe system, where the electrical conductivity decreases with the increase in ZnTe content.[25] In this study, we demonstrate that the increase in the electrical conductivity and n were caused by the nucleation and growth of the Ga_2Te_3 secondary phase. The formation of Ga_2Te_3 removes Te from the PbTe matrix causing deficiency and nonstoichiometry, which increases the number of electron carriers acting as an n-type dopant. This will be further discussed in the following sections.

The Seebeck coefficients for the $Pb_{0.975}Ga_{0.025}Te$–x%ZnTe samples increased gradually with temperature and reached the highest value of approximately -261 µV K^{-1} at 873 K for the x = 0.25 sample (see Figure 2b). In contrast to the electrical conductivity, the Seebeck coefficients decreased with increasing ZnTe content. Specifically, the room temperature Seebeck coefficients decreased from approximately -130 µV K^{-1} for the x = 0.5 sample to approximately -93 µV K^{-1} for the x = 0.75 sample. As shown in Figure 2c, the Pisarenko relation between the Seebeck coefficient and Hall carrier density shows that the density of states (DOS) effective mass for the $Pb_{0.975}Ga_{0.025}Te$–x%ZnTe samples is approximately 0.35 m_e

(black curve) at room temperature. This DOS effective mass is greater than that of a ~0.25 m_e I-doped PbTe–ZnTe.[25]

The temperature dependence of the power factors for the $Pb_{0.975}Ga_{0.025}Te–x\%ZnTe$ samples is plotted in Figure 2d. The values of the power factors exceeded 25 µW $cm^{-1}K^{-2}$ for all samples at room temperature and were greater than 15 µW $cm^{-1}K^{-2}$ over the entire test range. In the high-temperature range of $T > 623$ K, the ZnTe-alloyed samples exhibited higher power factor values (16–28 µW $cm^{-1}K^{-2}$) compared with the reference $Pb_{0.975}Ga_{0.025}Te$ (15–24 µW $cm^{-1}K^{-2}$). Moreover, $Pb_{0.975}Ga_{0.025}Te–0.25\%ZnTe$ indicated the highest value of ~35 µW $cm^{-1}K^{-2}$ at 373 K.

Thermal conductivity The total thermal conductivity as a function of temperature is shown in Figure 3a. The room temperature κ_{tot} increased as the ZnTe content increased from ~2.72 $Wm^{-1}K^{-1}$ for $Pb_{0.975}Ga_{0.025}Te$ to 3.29 $Wm^{-1}K^{-1}$ for the x = 0.75 sample; this trend is attributed to the increase in the electronic contribution to the heat transport. The κ_{tot} for all samples decreased with increasing temperature and exhibited the lowest value of ~1.07 $Wm^{-1}K^{-1}$ at 823 K for $Pb_{0.975}Ga_{0.025}Te–0.5\%ZnTe$.

Next, κ_{lat} was calculated using the formula $\kappa_{lat} = \kappa_{tot} - \kappa_{ele}$, and the results are shown in Figure 3b. Based on the Wiedemann–Franz relation, κ_{ele} was estimated using the equation $\kappa_{ele} = L\sigma T$ (L is the Lorenz number, $L = 1.5 + \exp[-|S|/116] \times 10^{-8}$ V^2K^{-2}).[36] For the ZnTe-alloyed samples, its κ_{lat} was lower than that of $Pb_{0.975}Ga_{0.025}Te$ over the entire temperature range. In detail, the $Pb_{0.975}Ga_{0.025}Te–0.5\%ZnTe$ sample indicated the lowest κ_{lat} of 1.28 $Wm^{-1}K^{-1}$, i.e., a reduction by ~26% compared with that of $Pb_{0.975}Ga_{0.025}Te$ (1.67 $Wm^{-1}K^{-1}$) at room temperature. As temperature increased, κ_{lat} declined to ~0.56 $Wm^{-1}K^{-1}$ at 673 K, which is lower than those of n- and p-type PbTe-based thermoelectric materials with relatively low alloy content (Figure S9, Supporting Information).[7, 13, 15, 19, 37, 38] Such a significant reduction in κ_{lat} with only 0.5% ZnTe alloying is extraordinary. Microstructure analysis and density functional theory calculations were performed to investigate the inner mechanism of this unusual phenomenon.

Microstructure analysis The microstructure of $Pb_{0.975}Ga_{0.025}Te–0.25\%ZnTe$ was

investigated via scanning/transmission electron microscopy (S/TEM), as shown in Figures 4a-4b. Figure 4a shows a typical low-magnification high-angle annular dark field (HAADF) image of the specimen, showing primarily the z-contrast from the sample. A significant number of faceted nanocrystals ranging from to 30–200 nm with a darker contrast was embedded in the matrix, as indicated by the red arrows. Chemical analysis with energy dispersive X-ray spectroscopy mappings (Figure 4b) further indicated that the nanocrystals were abundant in Ga and deficient in Pb. However, they showed no significant difference in terms of Te and Zn concentrations compared with the PbTe matrix. To further reveal the orientation relationship between the precipitate and matrix, we performed high-resolution TEM analysis on one of the mid-sized nanocrystals. As shown in Figure 4c, the nanocrystal exhibited a rectangular shape with a width of ~50 nm and a length of ~100 nm. The Moiré fringes along the horizontal direction indicate coherency between the two phases. The coherent embedding of the nanocrystals can enhance phonon scattering without affecting charge transport.[39] Figure 4d shows the corresponding selected area electron diffraction pattern in Figure 4c. The main diffraction spots can be indexed to the rock-salt PbTe phase (space group $Fm\overline{3}m$) along the [110] zone axis, as highlighted in red; the additional spots next to the main spots are assigned to Ga_2Te_3(space group: $F\overline{4}3m$). The lattice relationship between the two phases is $(2\overline{2}0)_{Ga2Te3}//(2\overline{2}0)_{PbTe}$, a misfit between which introduces significant strain and distortion. It is well known that the type of nanostructure present in the $Pb_{0.975}Ga_{0.025}Te$–0.25%ZnTe sample is favorable for maintaining superb electrical transport properties while significantly disrupting phonon propagation to reduce κ_{lat}.[39]

DFT calculations Based on our previous studies[13, 40-42] and the significantly reduced κ_{lat}, we analyzed the local atomic configurations of Zn and Ga doped in the host of PbTe. We discovered that the Zn atom preferred an energetically more favorable configuration, where the Zn atoms were distorted off-center from the appropriate octahedral position (Figure S10, Supporting Information). This is attributed to the small size of the Zn atom at the Pb site in the rock-salt PbTe structure, as well as the

strong preference for a tetrahedral coordination geometry of Zn^{2+}, particularly when the Zn atom is bonded to chalcogenide anions. As shown in Figure S10 (Supporting Information), the total energy of a Zn atom in an off-center position from the ideal octahedral site is slightly lower than that of Zn in the center position. The distortion of Zn in PbTe is similar to that of previous examples of Ge in PbQ (Q = Te and Se), Hg, and Cd in PbSe.[13, 40-42] Energetically, these off-centered atoms shift away from their appropriate sites along the [111] direction. It is suggested theoretically that Zn shifts from the regular octahedral site by approximately 0.36 Å, which is the largest displacement compared with those of the other off-centered elements in different crystalline matrices, as shown in Table 1. As reported previously, Ga in PbTe[34] prefers a distorted off-center position in PbTe. However, the Ga distortion magnitude is much smaller than that of the single Zn case. To investigate the effects of co-doping Zn and Ga on the κ_{lat} of PbTe, we further performed phonon dispersion calculations to compare the results with those from single Zn doping. For the Ga-doped and Zn-alloyed PbTe, the Zn and Ga atoms preferred to form a ZnGa substitution complex, where the Zn and Ga atoms were the nearest neighbors to each other. Based on the phonon dispersions, we evaluated the decrease in κ_{lat} upon the addition of a single Zn and a ZnGa complex. Similar to the previous case involving Ge or Cd in PbSe,[40, 42] the κ_{lat} of Zn doped in PbTe exhibited a substantial decrease. As shown in Figure S12 (Supporting Information), the single off-centered Zn addition induced a κ_{lat} reduction of approximately 10% at 300 K. By contrast, Ga doping and Zn alloying resulted in a reduction of approximately 22%. This significant decrease can be attributed to several factors. Beyond the mass fluctuation of Zn and Ga introduction, the calculated average phonon velocity *LA* branch of the ZnGa case (approximately 2350 m s^{-1}) was much smaller than that of pure PbTe (3160 m s^{-1}). By contrast, the off-centered Zn induced a relatively large atomic local strain, resulting in longer bond lengths of Pb–Te compared with those of regular cases; hence, relatively lower Pb vibration frequencies were induced. The low-frequency peak of the Pb phonon DOS is characterized as a left shift to a lower frequency, as shown in Figure S11b

(Supporting Information). Moreover, in the ZnGa complex case, the Ga atom generated low-frequency optical vibration modes, as shown at the Γ point with a frequency of approximately 7 cm^{-1}. This model exhibited a small peak in the phonon DOS in the extremely low frequency range (Figure 5), which is attributed to the off-centered Zn atom yielding a relatively loose atomic environment for Ga in the ZnGa complex. Hence, the off-centered Zn and related ZnGa complex contributed significantly to κ_{lat} reduction.

Additionally, we investigated the electronic band structure of PbTe with off-centered Ga and Zn atoms. For the Zn-alloyed PbTe, the conduction and valence bands of PbTe did not change significantly with respect to the Pb 6p and Te 5p states (Figure 6). For the Ga-doped and Zn-alloyed PbTe, the Ga atom addition introduced additional gap states that crossed the Fermi level near the Γ and K points.[43, 44] This phenomenon occurred similarly in the corresponding DOS, where the two peaks of the Ga 4s state significantly overlapped the Te 5p state at the top of the valence band and overlapped the Pb 6p state at the conduction band minimum. Additionally, the gap states induced by Ga enhanced the electronic transport properties of $Pb_{0.975}Ga_{0.025}Te–x\%ZnTe$.[13]

Figure of merit With the simultaneous enhanced power factor and reduced thermal conductivity, ZnTe alloying improved the thermoelectric performance of the n-type Ga-doped PbTe (Figure 7a). The highest ZT of ~1.55 at 723 K was demonstrated by $Pb_{0.975}Ga_{0.025}Te–0.25\%ZnTe$, i.e., ~30% higher than ~1.20 by the $Pb_{0.975}Ga_{0.025}Te$ sample. The $Pb_{0.975}Ga_{0.025}Te–0.25\%ZnTe$ compound indicated a record high ZT_{avg} ~1.26 (Figure 7b), which was higher than those of other top-performing n-type PbTe-based thermoelectric materials.[19, 20, 33, 45-48] In fact, the value was approximately the ZT_{avg} value of ~1.58 for the top p-type PbTe material over the range of 400–873 K.[23] ZT_{avg} is more important than a high peak ZT value during device fabrication for achieving maximum conversion efficiency. A theoretical η of ~14% for T_C = 400 K and T_H = 873 K were estimated for $Pb_{0.975}Ga_{0.025}Te–0.25\%ZnTe$ based on the record high ZT_{avg}. Combined with the top p-type PbTe material, the ZnTe-alloyed and Ga-

doped n-type PbTe is an ideal pair of material for developing highly efficient thermoelectric devices.

CONCLUSIONS

ZnTe-alloyed and Ga-doped n-type PbTe samples were successfully synthesized and investigated to uncover their promising thermoelectric properties as compared with their p-type counterparts for real-world device applications. In regard to the isoelectronic substitution of Pb in the PbTe matrix, discordant Zn with the largest lattice displacement significantly enhanced the thermoelectric performance of Ga-doped PbTe: (i) Zn enhanced σ and n by the induced Ga_2Te_3 secondary phase, thereby generating Te deficiencies in the matrix; (ii) Zn enabled a relatively loose atomic environment for Ga, which resulted in low-frequency optical vibration modes and significantly reduced κ_{lat}; (iii) Zn induced coherent Ga_2Te_3 nanocrystals, which further impeded phonon propagation without affecting charge transport. Finally, a record high ZT_{avg} of ~1.26 from 400 to 873 K with a maximum ZT of ~1.55 at 723 K was obtained by $Pb_{0.975}Ga_{0.025}Te$–0.25%ZnTe. Owing to the high ZT_{avg} value of $Pb_{0.975}Ga_{0.025}Te$–0.25%ZnTe, its theoretical efficiency was estimated to be ~14%. Combined with the high performance of p-type PbTe, the abovementioned results indicate that PbTe is an excellent thermoelectric material for use in high-efficiency thermoelectric generators.

Author contribution

Z. L., Z. Z., Q. Y and M. G. K. conceived of and planned the experiments. Z. L. prepared the samples and carried out thermoelectric experiments. S. C. and V. P. D. conducted TEM measurement of the samples. Hall measurements. S. H. and C. W. carried out the DFT calculations. T. P. B. and C. U. carried out the Hall measurements. Z. L., Z. Z., Q. Y., and M. G. K. interpreted all results and wrote and edited the manuscript. All authors have reviewed, discussed and approved the results and conclusions of this article.

Conflict of interest

The authors declare no conflict of interest.

REFERENCES

1.   G. Tan, L.-D. Zhao and M. G. Kanatzidis, *Chem. Rev.*, 2016, **116**, 12123-12149.

2.   G. J. Snyder and E. S. Toberer, *Nat. Mater.*, 2008, **7**, 105.

3.   L.-D. Zhao, S.-H. Lo, Y. Zhang, H. Sun, G. Tan, C. Uher, C. Wolverton, V. P. Dravid and M. G. Kanatzidis, *Nature*, 2014, **508**, 373-377.

4.   K. F. Hsu, S. Loo, F. Guo, W. Chen, J. S. Dyck, C. Uher, T. Hogan, E. K. Polychroniadis and M. G. Kanatzidis, *Science*, 2004, **303**, 818-821.

5.   Z.-Z. Luo, S. Hao, S. Cai, T. P. Bailey, G. Tan, Y. Luo, I. Spanopoulos, C. Uher, C. Wolverton, V. P. Dravid, Q. Yan and M. G. Kanatzidis, *J. Am. Chem. Soc.*, 2019, **141** , 6403-6412.

6.   Z.-Z. Luo, Y. Zhang, C. Zhang, H. T. Tan, Z. Li, A. Abutaha, X.-L. Wu, Q. Xiong, K. A. Khor, K. Hippalgaonkar, J. Xu, H. H. Hng and Q. Yan, *Adv. Energy Mater.*, 2017, **7**, 1601285.

7.   Z.-Z. Luo, X. Zhang, X. Hua, G. Tan, T. P. Bailey, J. Xu, C. Uher, C. Wolverton, V. P. Dravid, Q. Yan and M. G. Kanatzidis., *Adv. Funct. Mater.*, 2018, **0**, 1801617.

8.   A. D. LaLonde, Y. Pei, H. Wang and G. Jeffrey Snyder, *Materials Today*, 2011, **14**, 526-532.

9.   Y. Tang, Z. M. Gibbs, L. A. Agapito, G. Li, H.-S. Kim, M. B. Nardelli, S. Curtarolo and G. J. Snyder, *Nat. Mater.*, 2015, **14**, 1223-1228.

10. Z.-Z. Luo, S. Cai, S. Hao, T. P. Bailey, I. Spanopoulos, Y. Luo, J. Xu, C. Uher, C. Wolverton, V. P. Dravid, Q. Yan and M. G. Kanatzidis, *Angew. Chem. Int. Ed. Engl.*, 2021, **60**, 268-273.

11. K. Biswas, J. He, Q. Zhang, G. Wang, C. Uher, V. P. Dravid and M. G. Kanatzidis, *Nat. Chem.*, 2011, **3**, 160-166.

12. L.-D. Zhao, G. Tan, S. Hao, J. He, Y. Pei, H. Chi, H. Wang, S. Gong, H. Xu, V. P. Dravid, C. Uher, G. J. Snyder, C. Wolverton and M. G. Kanatzidis, *Science*, 2016, **351**, 141-144.

13. Z.-Z. Luo, S. Cai, S. Hao, T. P. Bailey, X. Su, I. Spanopoulos, I. Hadar, G. Tan, Y. Luo, J. Xu, C. Uher, C. Wolverton, V. P. Dravid, Q. Yan and M. G. Kanatzidis, *J. Am. Chem. Soc.*, 2019, **141**, 16169-16177.

14. Y. Wu, Z. Chen, P. Nan, F. Xiong, S. Lin, X. Zhang, Y. Chen, L. Chen, B. Ge and Y. Pei, *Joule*, 2019, **3**, 1276-1288.

15. L.-D. Zhao, H. J. Wu, S. Q. Hao, C. I. Wu, X. Y. Zhou, K. Biswas, J. Q. He, T. P. Hogan, C. Uher, C. Wolverton, V. P. Dravid and M. G. Kanatzidis, *Energy Environ. Sci.*, 2013, **6**, 3346.

16. D. Wu, L.-D. Zhao, X. Tong, W. Li, L. Wu, Q. Tan, Y. Pei, L. Huang, J.-F. Li, Y. Zhu, M. G. Kanatzidis and J. He, *Energy Environ. Sci.*, 2015, **8**, 2056-2068.

17. H. J. Wu, L.-D. Zhao, F. S. Zheng, D. Wu, Y. L. Pei, X. Tong, M. G. Kanatzidis and J. Q. He, *Nat Commun*, 2014, **5**, 4515.

18. D. Wang, Y. Qin, S. Wang, Y. Qiu, D. Ren, Y. Xiao and L.-D. Zhao, *Annalen der Physik*, 2019**, 532**, 1900421.

19. G. Tan, C. C. Stoumpos, S. Wang, T. P. Bailey, L.-D. Zhao, C. Uher and M. G. Kanatzidis, *Adv. Energy Mater.*, 2017, **7**, 1700099.

20. X. Su, S. Hao, T. P. Bailey, S. Wang, I. Hadar, G. Tan, T. B. Song, Q. Zhang, C. Uher, C. Wolverton, *Adv. Energy Mater.*, 2018, **8**, 1800659.

21. A. D. LaLonde, Y. Pei and G. J. Snyder, *Energy Environ. Sci.*, 2011, **4**, 2090-2096.

22. Y. Pei, Z. M. Gibbs, A. Gloskovskii, B. Balke, W. G. Zeier and G. J. Snyder, *Adv. Energy Mater.*, 2014, **4**, 1400486.

23. G. Tan, F. Shi, S. Hao, L.-D. Zhao, H. Chi, X. Zhang, C. Uher, C. Wolverton, V. P. Dravid and M. G. Kanatzidis, *Nat. Commun.*, 2016, **7**, 12167.

24. K. Ahn, K. Biswas, J. He, I. Chung, V. Dravid and M. G. Kanatzidis, *Energy Environ. Sci.*, 2013, **6**, 1529.

25. P. K. Rawat, B. Paul and P. Banerji, *ACS Appl. Mater. Interfaces*, 2014, **6**, 3995-4004.

26. J.-H. Bahk and A. Shakouri, *Appl. Phys. Lett.*, 2014, **105**, 052106.

27. B. J. Sealy and A. J. Crocker, *J. Mater. Sci.*, 1973, **8**, 1731-1736.

28. K. Ahn, H. Shin, J. Im, S. H. Park and I. Chung, *ACS Appl. Mater. Interfaces*, 2017, **9**, 3766-3773.

29. T. L. Chu, S. S. Chu, F. Firszt and C. Herrington, *J. Appl. Phys.*, 1986, **59**, 1259-1263.

30. J. Zhang, D. Wu, D. He, D. Feng, M. Yin, X. Qin and J. He, *Adv. Mater.*, 2017, **29**, 1703148.

31. S. Wang, Y. Xiao, Y. Chen, S. Peng, D. Wang, T. Hong, Z. Yang, Y. Sun, X. Gao and L.-D. Zhao, *Energy Environ. Sci.*, 2021, **14**, 451-461.

32. Y. Pei, A. D. LaLonde, H. Wang and G. J. Snyder, *Energy Environ. Sci.*, 2012, **5**, 7963-7969.

33. P. Jood, M. Ohta, M. Kunii, X. Hu, H. Nishiate, A. Yamamoto and M. G. Kanatzidis, *J. Mater. Chem. C*, 2015, **3**, 10401-10408.

34. S. Sarkar, X. Hua, S. Hao, X. Zhang, T. P. Bailey, T. J. Slade, P. Yasaei, R. J. Korkosz, G. Tan, C. Uher, V. P. Dravid, C. Wolverton and M. G. Kanatzidis, *Chem. Mater.*, 2021, **33**, 1842-1851.

35. Y. Xiao, W. Li, C. Chang, Y. Chen, L. Huang, J. He and L.-D. Zhao, *J. Alloys Compd.*, 2017, **724**, 208-221.

36. H.-S. Kim, Z. M. Gibbs, Y. Tang, H. Wang and G. J. Snyder, *APL Materials*, 2015, **3**, 041506.

37. J. Luo, L. You, J. Zhang, K. Guo, H. Zhu, L. Gu, Z. Yang, X. Li, J. Yang and W. Zhang, *ACS Appl. Mater. Interfaces*, 2017, **9**, 8729-8736.

38. S. Sarkar, X. Zhang, S. Hao, X. Hua, T. P. Bailey, C. Uher, C. Wolverton, V. P. Dravid and M. G. Kanatzidis, *ACS Energy Letters*, 2018, **3**, 2593-2601.

39. K. Biswas, J. He, Q. Zhang, G. Wang, C. Uher, V. P. Dravid and M. G. Kanatzidis, *Nat Chem*, 2011, **3**, 160-166.

40. Z.-Z. Luo, S. Hao, X. Zhang, X. Hua, S. Cai, G. Tan, T. P. Bailey, R. Ma, C. Uher, C. Wolverton, V. P. Dravid, Q. Yan and M. G. Kanatzidis, *Energy Environ. Sci.*, 2018, **11**, 3220-3230.

41.   J. M. Hodges, S. Hao, J. A. Grovogui, X. Zhang, T. P. Bailey, X. Li, Z. Gan, Y. Y. Hu, C. Uher, V. P. Dravid, C. Wolverton and M. G. Kanatzidis, *J. Am. Chem. Soc.*, 2018, **140**, 18115-18123.

42.   S. Cai, S. Hao, Z.-Z. Luo, X. Li, I. Hadar, T. P. Bailey, X. Hu, C. Uher, Y.-Y. Hu, C. Wolverton, V. P. Dravid and M. G. Kanatzidis, *Energy Environ. Sci.*, 2020, **13**, 200-211.

43.   K. Hoang and S. D. Mahanti, *Phys. Rev. B*, 2008, **78**, 085111.

44.   S. Ahmad, S. D. Mahanti, K. Hoang and M. G. Kanatzidis, *Phys. Rev. B*, 2006, **74**, 155205.

45.   Y. Xiao, H. Wu, D. Wang, C. Niu, Y. Pei, Y. Zhang, I. Spanopoulos, I. T. Witting, X. Li, S. J. Pennycook, G. J. Snyder, M. G. Kanatzidis and L.-D. Zhao, *Adv. Energy Mater.*, 2019, **9**, 1900414.

46.   Y. Xiao, H. Wu, W. Li, M. Yin, Y. Pei, Y. Zhang, L. Fu, Y. Chen, S. J. Pennycook, L. Huang, J. He and L.-D. Zhao, *J. Am. Chem. Soc.*, 2017, **139**, 18732-18738.

47.   Q. Zhang, E. K. Chere, Y. Wang, H. S. Kim, R. He, F. Cao, K. Dahal, D. Broido, G. Chen and Z. Ren, *Nano Energy*, 2016, **22**, 572-582.

48.   D. Wang, Y. Qin, S. Wang, Y. Qiu, D. Ren, Y. Xiao and L.-D. Zhao, *Annalen der Physik*, 2020, **532**, 1900421.

49.   M. Dutta, R. K. Biswas, S. K. Pati and K. Biswas, *ACS Energy Letters*, 2021, **6**, 1625-1632.

50.   H. Xie, X. Su, S. Hao, C. Zhang, Z. Zhang, W. Liu, Y. Yan, C. Wolverton, X. Tang and M. G. Kanatzidis, *J. Am. Chem. Soc.*, 2019, **141**, 18900-18909.
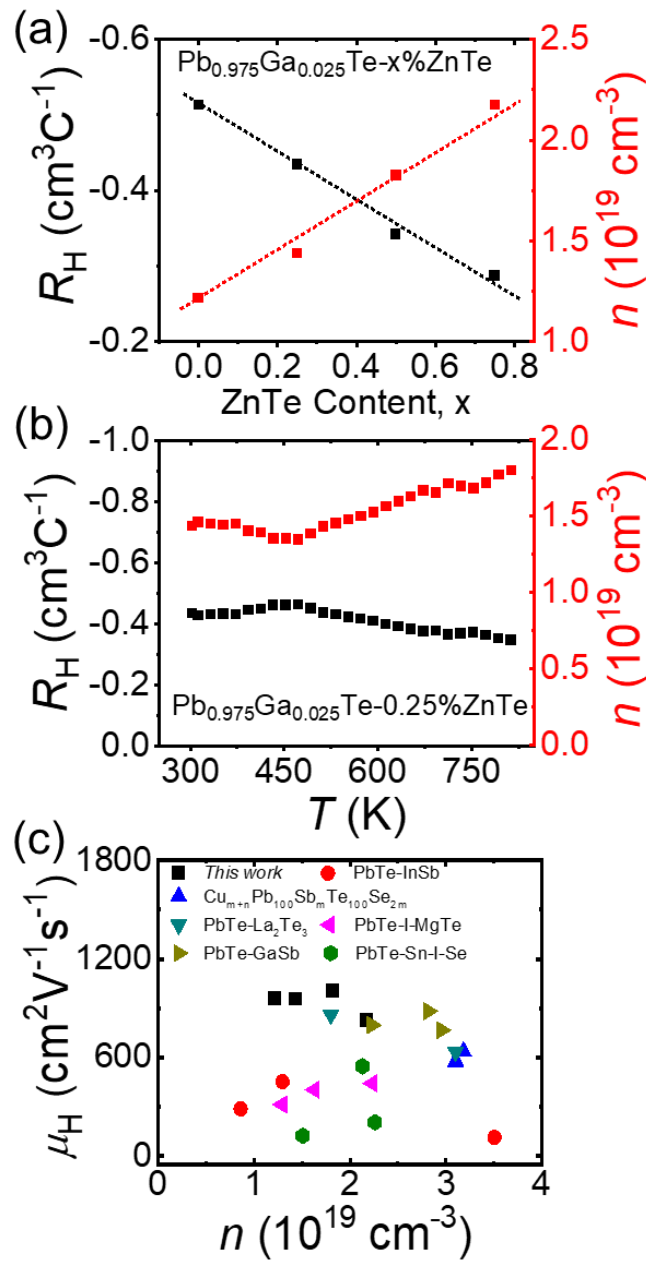
Figure 1. (a) Hall coefficient, R_H, and charge carrier concentration, n, at 300 K for $Pb_{0.975}Ga_{0.025}Te–x\%ZnTe$; (b) temperature-dependent R_H and n for $Pb_{0.975}Ga_{0.025}Te–0.25\%ZnTe$. (c) Comparison of carrier mobility, μ_H, from this study with those of known high-performance PbTe-based samples: PbTe-InSb,[30] $Cu_{m+n}Pb_{100}Sb_mTe_{100}Se_{2m}$,[31] $PbTe-La_2Te_3$,[32] $PbTe_{1–x}I_{x–y}MgTe1\%$,[33] PbTe-GaSb[34], and $Pb_{1–x}Sn_xTe_{0.997–y}Se_yI_{0.003}$.[35]
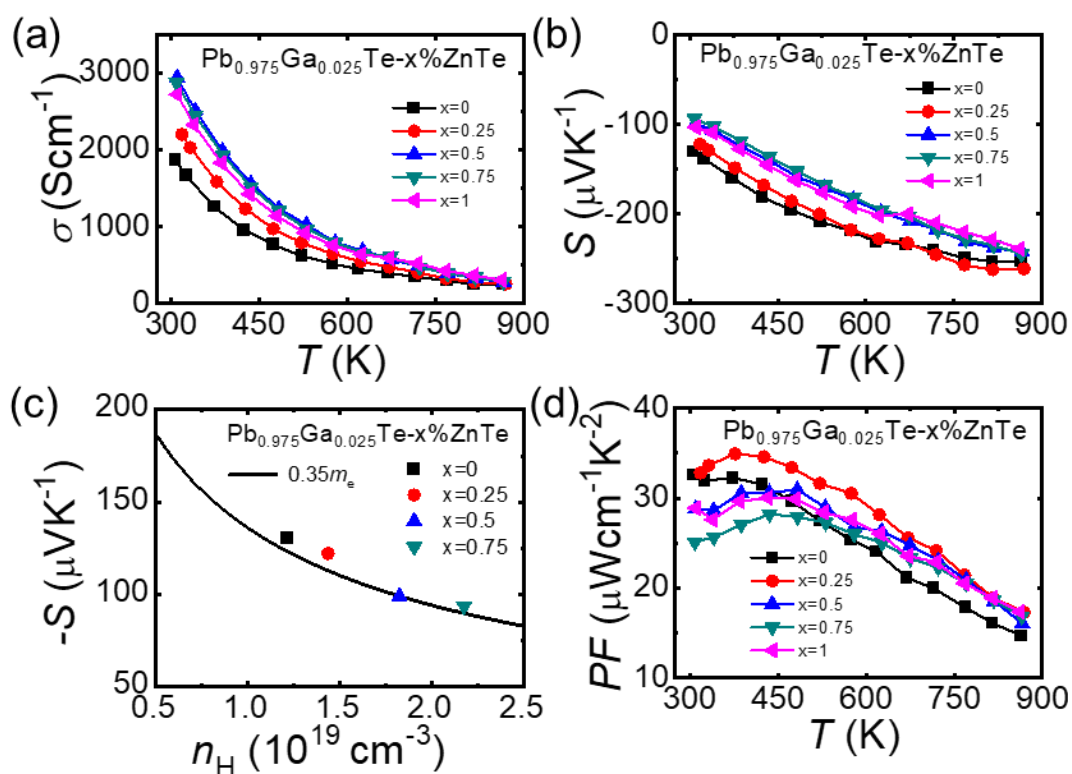
Figure 2. Electronic properties as a function of temperature for $Pb_{0.975}Ga_{0.025}Te$–x%ZnTe (x = 0, 0.25, 0.5, 0.75, and 1): (a) Electrical conductivity, σ; (b) Seebeck coefficient, S; (c) Seebeck coefficient (-S) as a function of Hall carrier concentration at 300 K; (d) power factor, PF. Solid curve in (c) shows the theoretical Pisarenko curve for n-type PbTe with effective mass of electrons of 0.35 m_e.
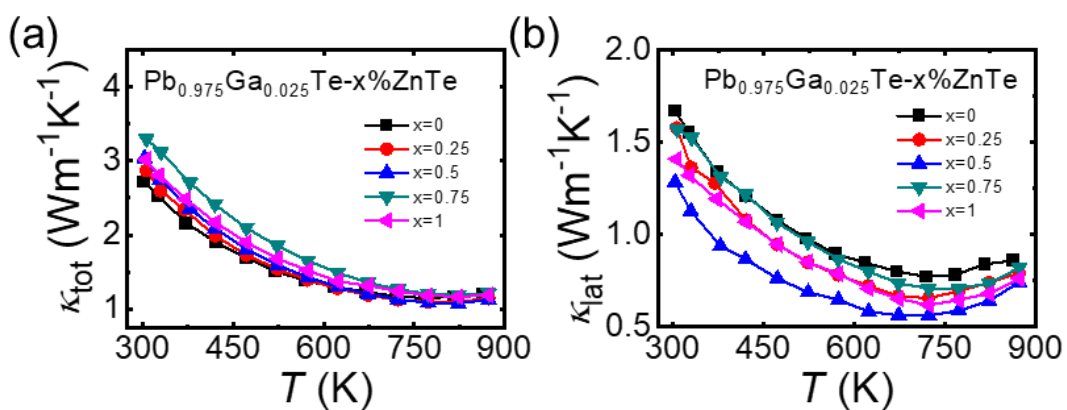

Figure 3. Thermal properties as a function of temperature for $Pb_{0.975}Ga_{0.025}Te$–x%ZnTe (x = 0, 0.25, 0.5, 0.75, and 1): (a) Total thermal conductivity, κ_{tot} and (b) lattice thermal conductivity, κ_{lat}.
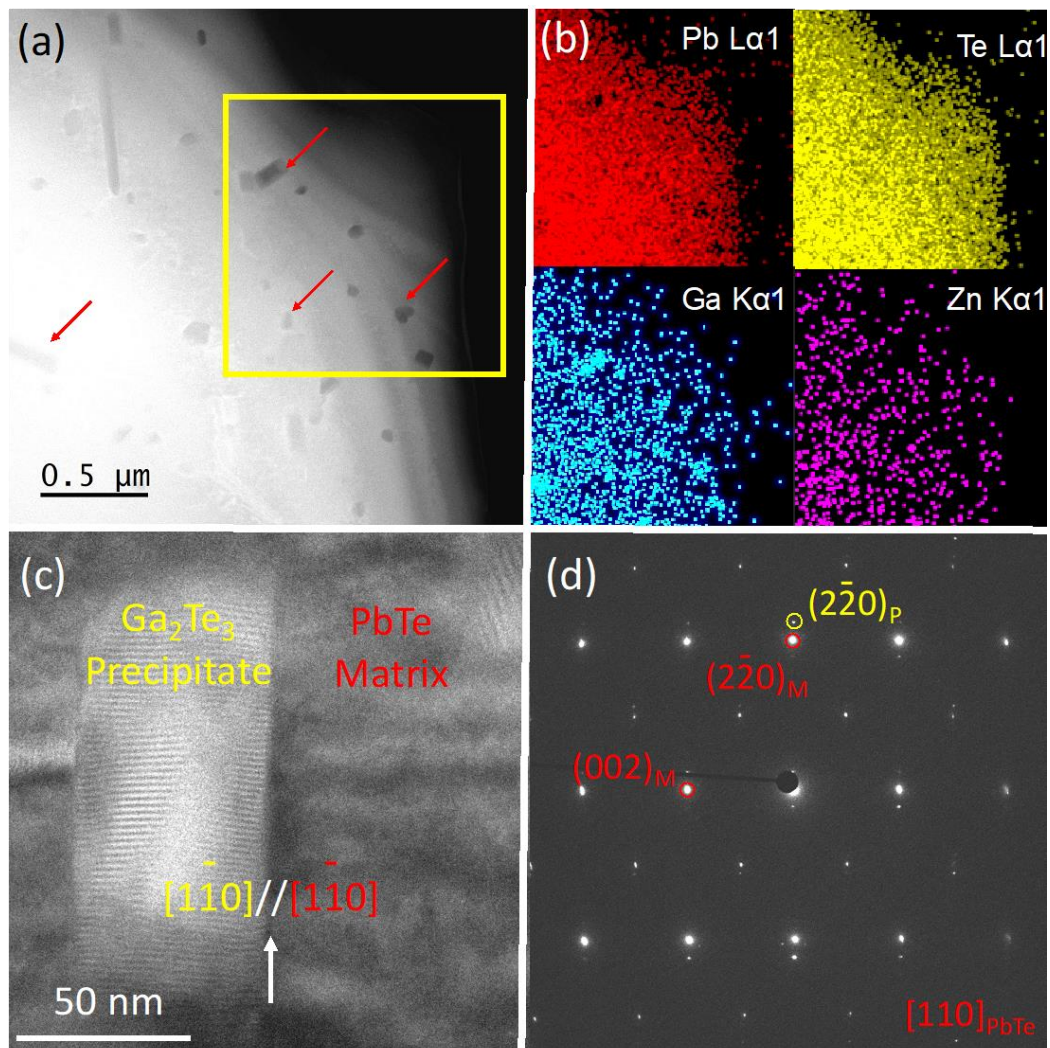
Figure 4. S/TEM analyses of Pb$_{0.975}$Ga$_{0.025}$Te-0.25%ZnTe sample. (a) HAADF image and (b) the corresponding EDS mappings. (c) High-resolution TEM image of one Ga$_2$Te$_3$ nanocrystal embedded in PbTe matrix along [110] zone axis and (d) corresponding selected electron diffraction pattern of (c).
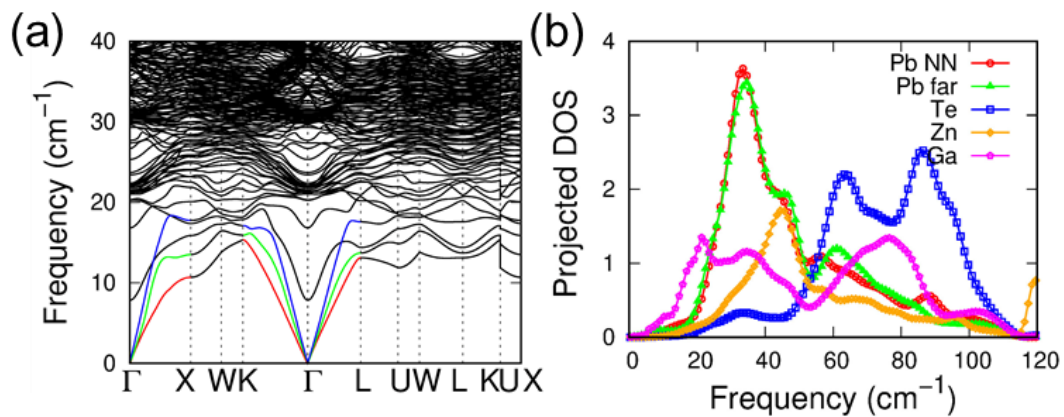
Figure 5. (a) Phonon dispersion curves (green and red curves for transverse, and blue curves for longitudinal acoustic branches) and (b) projected phonon density of states (DOS) for discordant Ga-doped and Zn-alloyed PbTe. ''Pb NN'' represents six Pb atoms that are next nearest neighbors to discordant Zn atom within supercell, whereas other Pb atoms are denoted as ''Pb far.''
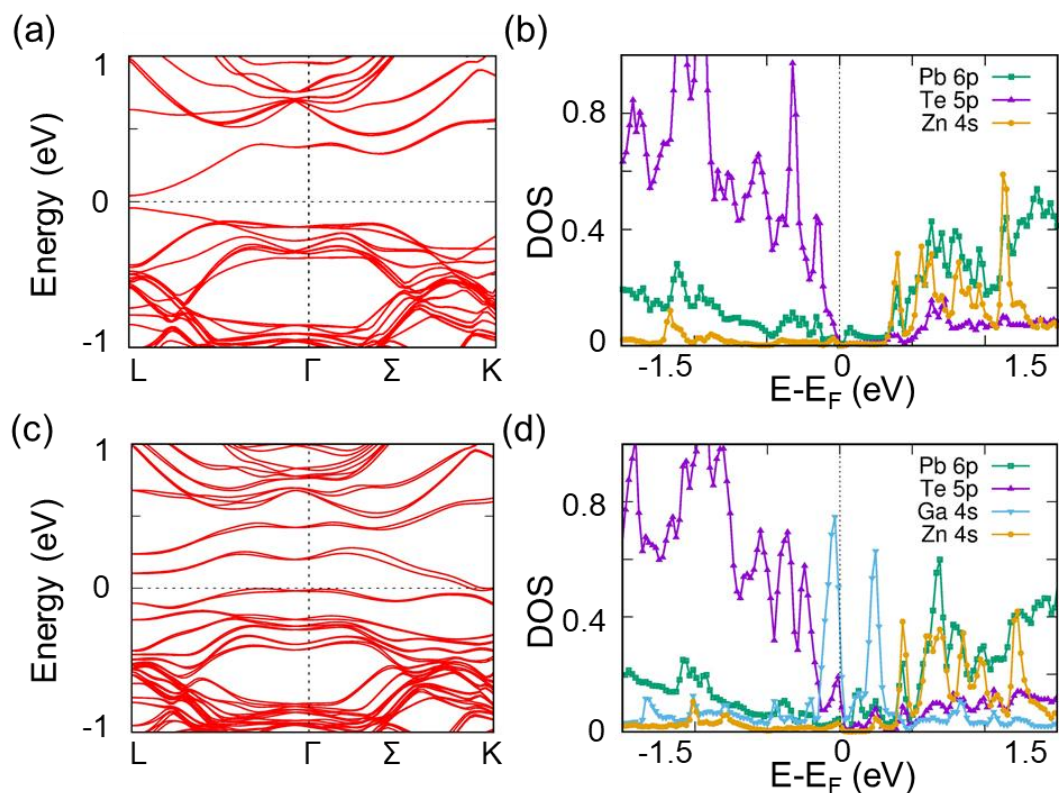

Figure 6. Electronic energy band structure of (a) ZnTe-alloyed PbTe and (c) Ga-doped and ZnTe-alloyed PbTe for Ga and Zn off-centered model; (b) and (d) show corresponding projected density of states of (a) and (c), respectively.
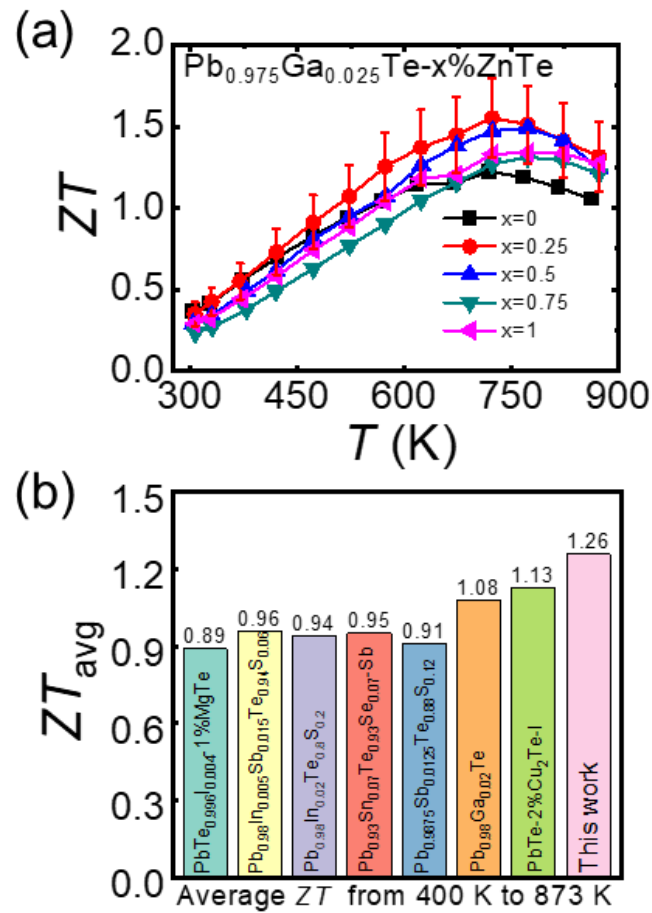
Figure 7. (a) Figure of merit, ZT, as a function of temperature for $Pb_{0.975}Ga_{0.025}Te$–x%ZnTe (x = 0, 0.25, 0.5, 0.75, and 1), and (b) comparison of ZT_{avg} values at 400–873 K for top-performing n-type PbTe-based thermoelectric materials.[19, 20, 33, 45-48]

Table 1. Comparison of off-centered displacements for the alloying elements in different crystalline matrixes

Alloyed element	off-centered displacement (Å)	Matrix	Ref.
Zn	0.36	PbTe	This work
Ge	0.25	PbTe	Ref.[13]
Ga	0.08	PbTe	Ref.[13]
Gd	0.20	PbTe	Ref.[49]
Ge	0.30	PbSe	Ref.[40]
Hg	0.20	PbSe	Ref.[41]
Cd	0.01	PbSe	Ref.[42]
Ge	0.14	PbS	Unpublished
In	0.12	$CuFeS_2$	Ref.[50]